



## Modulating the electronic structure of NiFe hydroxide by Zr doping enables industrial-grade current densities for water oxidation

Rui Zhao<sup>a</sup>, Shuai Xu<sup>b</sup>, Dongyu Liu<sup>d</sup>, Liting Wei<sup>a</sup>, Suyi Yang<sup>a</sup>, Xueli Yan<sup>a</sup>, Yubin Chen<sup>a,\*</sup>, Zhaohui Zhou<sup>b,\*</sup>, Jinzhuan Su<sup>a</sup>, Liejin Guo<sup>a</sup>, Clemens Burda<sup>c,\*</sup>

<sup>a</sup> International Research Center for Renewable Energy, State Key Laboratory of Multiphase Flow in Power Engineering, Xi'an Jiaotong University, Xi'an 710049, China

<sup>b</sup> Department of Chemical Engineering, School of Water and Environment, Key Laboratory of Subsurface Hydrology and Ecological Effects in Arid Region, Ministry of Education, Chang'an University, Xi'an 710064, China

<sup>c</sup> Department of Chemistry, Case Western Reserve University, Cleveland, OH 44106, USA

<sup>d</sup> HSE University, Moscow 101000, Russia



### ARTICLE INFO

#### Keywords:

Water splitting  
Oxygen evolution reaction  
Hydrogen  
Electrocatalysis  
NiFe layered double hydroxide

### ABSTRACT

NiFe layered double hydroxide (LDH) is a non-noble benchmark catalyst for oxygen evolution reaction (OER). However, the mechanism of enhancing catalytic activities via incorporating foreign elements is still not resolved. Herein, we modulate the electronic structure of NiFe LDH by introducing high-valence Zr<sup>4+</sup> to synergistically improve catalytic activity. NiFeZr LDH requires overpotential of only 182 mV at 10 mA cm<sup>-2</sup> with Tafel slope of 38.6 mV dec<sup>-1</sup>. Impressively, it delivers 2000 mA cm<sup>-2</sup> at only 314 mV and has robust durability over 750 h. Operational Raman analysis reveals that the electron transfer after incorporating Zr<sup>4+</sup> inhibits oxidation of Ni<sup>2+</sup> ions and restrains phase transition from active  $\beta$ -NiOOH to  $\gamma$ -NiOOH during OER process. Guided by density functional theory (DFT) computations, Zr<sup>4+</sup> modulator promotes the rate-determining step from OH<sup>\*</sup> to O<sup>\*</sup> via optimizing the oxidation cycle at Fe active sites. This work provides a route for advancing electrocatalysts to meet industrial standards.

### 1. Introduction

Excessive consumption of fossil fuels has inevitably caused an energy crisis and environmental deterioration, which urges the utilization of renewable clean energy [1–3]. Hydrogen (H<sub>2</sub>), a kind of energy carrier with the highest energy density per unit mass and zero-carbon emission, has sparked a burning interest to replace fossil fuels for global carbon neutrality [4]. Water electrolysis, consisting of hydrogen evolution reaction (HER) and oxygen evolution reaction (OER), driven by renewable electricity such as solar, wind, and tide energy is a promising technology to produce green hydrogen [5]. However, the sluggish kinetics involving four-electron-proton transfer step of anodic OER, the high energy barrier, and the scarcity of noble-metal-based electrocatalysts such as RuO<sub>2</sub> and IrO<sub>2</sub> severely hamper large-scale hydrogen production [6,7]. Alternatively, NiFe layered double hydroxide (LDH) has been regarded as one of the most active OER electrocatalysts in alkaline media [8–10], which outperforms most non-noble ones like transition metal oxides [11], perovskites [12], spinels [13], and other transition-metal-based electrocatalysts [14]. Moreover, in the context of more advanced

research techniques, the origin of the appreciable OER activity of NiFe (oxy)hydroxide catalysts has gradually evolved from competing Ni vs. Fe active sites to the synergy of the two [8,15–17]. A clearer understanding of the microscopic catalytic mechanisms has profound implications for making rapid strides. Although NiFe LDH stands out among the non-precious metal-based catalysts, its water-splitting performance still has a gap in the demand for industrial water electrolysis.

Recently, some significant efforts have shown that the incorporation of a third transition metal atom such as V [18,19], Cr [20,21], Ce [22], Mo [23], Ta [24], W [25], etc. into NiFe or CoFe (oxy)hydroxide can effectively modulate the electronic structure of the 3d-metal matrix, further breaking the constraints of poor intrinsic activity. However, a series of key issues are still unclear about the underlying mechanism of elevating OER activity via doping with metal elements, such as the identification of real active intermediates or active sites. A convincing preliminary consensus has not yet been formed. Zr is an earth-abundant metal with varied oxidation states (+2, +3, and +4), and the common Zr<sup>4+</sup> can act as an incorporated modulator to facilitate the catalytic activity [26]. Wang's group [27] reported that the incorporation of Zr

\* Corresponding authors.

E-mail addresses: [ybchen@mail.xjtu.edu.cn](mailto:ybchen@mail.xjtu.edu.cn) (Y. Chen), [zzhlax@chd.edu.cn](mailto:zzhlax@chd.edu.cn) (Z. Zhou), [burda@case.edu](mailto:burda@case.edu) (C. Burda).

into  $\text{CoFe}_2\text{O}_4$  can optimize the adsorption energy for intermediates by tuning the nanosheet morphology and electronic structure, thus significantly improving the OER and HER activities. Similarly, Wang et al. [28] proposed that the OER activity of NiFe-MOFs was markedly enhanced after incorporating the high valence of Zr, resulting from the increased electrochemical surface area (ECSA) and the modulation of electronic structure around the Ni and Fe atoms. To the best of our knowledge, the incorporation of high-valence  $\text{Zr}^{4+}$  into NiFe LDH catalysts for OER has not been fully explored so far. Compared to a limited performance in the laboratory, there are few reports in which the industrial-scale high current density ( $>400 \text{ mA cm}^{-2}$ ) for water splitting was satisfied [29]. In particular, there have been no in-depth reports on tracking the structural evolution and four-step oxidation cycle at active sites for a NiFeZr LDH trimetallic catalyst during the OER process.

Herein, we developed an active NiFeZr LDH catalyst by incorporating the high-valence  $\text{Zr}^{4+}$  into NiFe LDH host layers via a facile hydrothermal method, which exhibited intrinsically exceptional OER activity at low and high current densities, outperforming the NiFe LDH benchmark catalyst. It was found that  $\text{Zr}^{4+}$  ions modulated the electronic structure of the parent Ni and Fe matrix and inhibited oxidative transitions from  $\text{Ni}^{\text{II}}\text{-O}$  to  $\text{Ni}^{\text{III}}\text{-O}$ , generating more active  $\beta\text{-NiOOH}$  phase. DFT calculations demonstrated that  $\text{Zr}^{4+}$  modulator induced a lower oxidation states of Fe active sites in NiFeZr LDH, thus optimizing the oxidation cycle energy in the four-electron transfer process.

## 2. Experimental section

### 2.1. Chemicals and materials

Ferric nitrate ( $\text{Fe}(\text{NO}_3)_3\cdot 9\text{H}_2\text{O}$ , analytical reagent), nickel nitrate ( $\text{Ni}(\text{NO}_3)_2\cdot 6\text{H}_2\text{O}$ , analytical reagent), zirconium nitrate ( $\text{Zr}(\text{NO}_3)_4\cdot 5\text{H}_2\text{O}$ , analytical reagent), urea ( $\text{CO}(\text{NH}_2)_2$ , analytical reagent), hydrochloric acid (HCl, 36 wt%), potassium hydroxide (KOH, guaranteed reagent), and ruthenium oxide ( $\text{RuO}_2$ , 99%) were purchased from Sinopharm Chemical Reagent Co., Ltd (SCRC). Nickel foam was purchased from KJ Group (China). Nafion solution (5 wt%) was purchased from Alfa Aesar®. All chemicals were used without further purification.

### 2.2. Synthesis of NiFeZr LDH electrode

The ultrathin layered double hydroxides NiFeZr LDHs in situ growing on NF were prepared by a facile one-pot hydrothermal method. In a typical procedure, NF (1 cm × 3 cm) was cleaned with 3 M HCl in an ultrasonic bath for 30 min, and then washed with deionized water and ethanol for 30 min, respectively. After drying at 60 °C for 12 h in vacuum, the cleaned NF was obtained. Meanwhile,  $\text{Ni}(\text{NO}_3)_2\cdot 6\text{H}_2\text{O}$  (0.4 mmol),  $\text{Fe}(\text{NO}_3)_3\cdot 9\text{H}_2\text{O}$  (0.4 mmol),  $\text{Zr}(\text{NO}_3)_4\cdot 5\text{H}_2\text{O}$  (0.4 mmol), and  $\text{CO}(\text{NH}_2)_2$  (5 mmol) were dissolved in deionized water (32 mL). After ultrasonication for 30 min, the aqueous solution and a piece of cleaned NF were transferred into a 40 mL Teflon-lined stainless-steel autoclave, which was sealed and maintained at 120 °C for 12 h, and then cooled to room temperature naturally. The prepared film electrode was ultrasonically rinsed with deionized water three times, and then dried at 60 °C for 8 h.

### 2.3. Synthesis of NiFe LDH, NiZr LDH, and $\text{Ni}(\text{OH})_2$ electrodes

The NiFe LDH, NiZr LDH, and  $\text{Ni}(\text{OH})_2$  electrodes were synthesized following the above method. For both NiFe LDH and NiZr LDH, the amount of  $\text{Ni}(\text{NO}_3)_2\cdot 6\text{H}_2\text{O}$  was replaced by 0.8 mmol. For  $\text{Ni}(\text{OH})_2$ , the amount of  $\text{Ni}(\text{NO}_3)_2\cdot 6\text{H}_2\text{O}$  was replaced by 1.2 mmol.

### 2.4. Synthesis of $\text{RuO}_2$ electrode

20 mg  $\text{RuO}_2$  powder and 50  $\mu\text{L}$  Nafion were dispersed in 950  $\mu\text{L}$  ethanol and sonicated for 30 min to prepare a homogeneous ink. The

$\text{RuO}_2$  electrode was prepared by coating the catalyst ink on a clean Ni foam substrate with a loading mass of about  $2.0 \text{ mg cm}^{-2}$ . Then, the electrode was dried at 60 °C for 8 h for an electrochemical test.

## 3. Results and discussion

### 3.1. Synthesis and structural characterization

The synthesis process for NiFeZr LDH is illustrated in Fig. 1a. The NiFeZr LDH was in situ grown on nickel foam (NF) via a one-pot hydrothermal method, and NiFe LDH, NiZr LDH, and  $\text{Ni}(\text{OH})_2$  were also synthesized as controls. The scanning electron microscopy (SEM) image of NiFeZr LDH (Fig. 1b and S1) displays that nanoflowers are composed of dense nanosheets, which is about 4–6 nm as characterized by atomic force microscopy (AFM) (Fig. 1c). Transmission electron microscopy (TEM) images of NiFeZr LDH (Fig. 1d) further confirm the uniformity of the ultra-thin nanosheets.

The X-ray diffraction (XRD) patterns of NiFe LDH are presented in Fig. S5. The diffraction peaks can be indexed to a hydrotalcite-like structure (JCPDS No. 04-0215). The diffraction peaks of NiFeZr LDH are consistent with the NiFe LDH, revealing that the crystal structure of NiFe LDH is well maintained after the incorporation of Zr. However, the slight negative shift of the diffraction peaks in NiFeZr LDH indicates a lattice expansion, owing to the larger ionic radius of  $\text{Zr}^{4+}$  (79 pm) than  $\text{Ni}^{2+}$  (69 pm) or  $\text{Fe}^{3+}$  (64 pm) [27]. This lattice distortion in NiFeZr LDH can give rise to increased strain and change the distance between adjacent metal cations in the host layer, causing the redistribution of electrons [24]. The Zr dopant could be successfully incorporated into the NiFe LDH laminates because of the well-matched hexa-coordination with the crystal structure of the hydrotalcite matrix [18]. Subsequently, the selected area electron diffraction SAED pattern (Fig. 1e) shows the diffraction rings indexed to the (012), (018), and (116) planes, which is consistent with the XRD pattern. Meanwhile, as illustrated in Fig. 1e, the high-angle annular dark-field scanning TEM (HAADF-STEM) image and the corresponding energy dispersive X-ray (EDX) elemental mapping confirm the uniform distribution of Ni, Fe, Zr, and O elements in NiFeZr LDH. Furthermore, the Ni:Fe:Zr molar ratio, measured by inductively coupled plasma mass spectrometry (ICP-MS), is 2.69:1.37:1 for NiFeZr LDH (Table S1).

### 3.2. Atomic structure and electronic interaction

X-ray photoelectron spectroscopy (XPS) was performed to explore the influence of the Zr dopant on the electronic structure of NiFe LDH. The survey XPS profiles (Fig. 2a) verify the co-existence of Ni, Fe, Zr, and O elements in NiFeZr LDH, which agree well with the EDX and ICP-MS analysis. The high-resolution Ni 2p spectra of NiFe LDH (Fig. 2b) are deconvoluted into two peaks at the binding energies of 873.7 eV and 856.1 eV corresponding to Ni 2p<sub>1/2</sub> and Ni 2p<sub>3/2</sub>, respectively, an indication of  $\text{Ni}^{2+}$  oxidation state. The observed  $\text{Ni}^0$  peak at 851.80 eV is attributed to the NF substrate. From the Fe 2p signal (Fig. 2c), the Fe 2p<sub>1/2</sub> and Fe 2p<sub>3/2</sub> peaks at 724.6 eV and 713.0 eV are observed in the NiFe LDH, indicating the existence of  $\text{Fe}^{3+}$ . The Ni 2p and Fe 2p peaks shift to the higher binding energies after incorporating  $\text{Zr}^{4+}$  ions, respectively, implying that high-valence  $\text{Zr}^{4+}$  triggers the redistribution of charges around Ni and Fe atoms [30,31]. This verifies the XRD analysis above. Fig. 2d presents the high-resolution Zr 3d spectrum of NiZr LDH, which is split into Zr 3d<sub>3/2</sub> and Zr 3d<sub>5/2</sub> peaks at 185.2 eV and 182.7 eV corresponding to  $\text{Zr}^{4+}$  species. The above results reveal that the introduction of  $\text{Zr}^{4+}$  ions modulates the electronic structure and chemical environment of the Ni and Fe matrix.

Our understanding of the changes in oxidation states of parent Ni and Fe atoms through valence-bond theory is summarized in the schematic diagram of the electron transfer via the bridging O atoms within NiFe LDH and NiFeZr LDH (Fig. 2e). For NiFe LDH, the dominant electron-electron repulsion occurs between  $\text{Ni}^{2+}$  and the bridging  $\text{O}^{2-}$  owing to

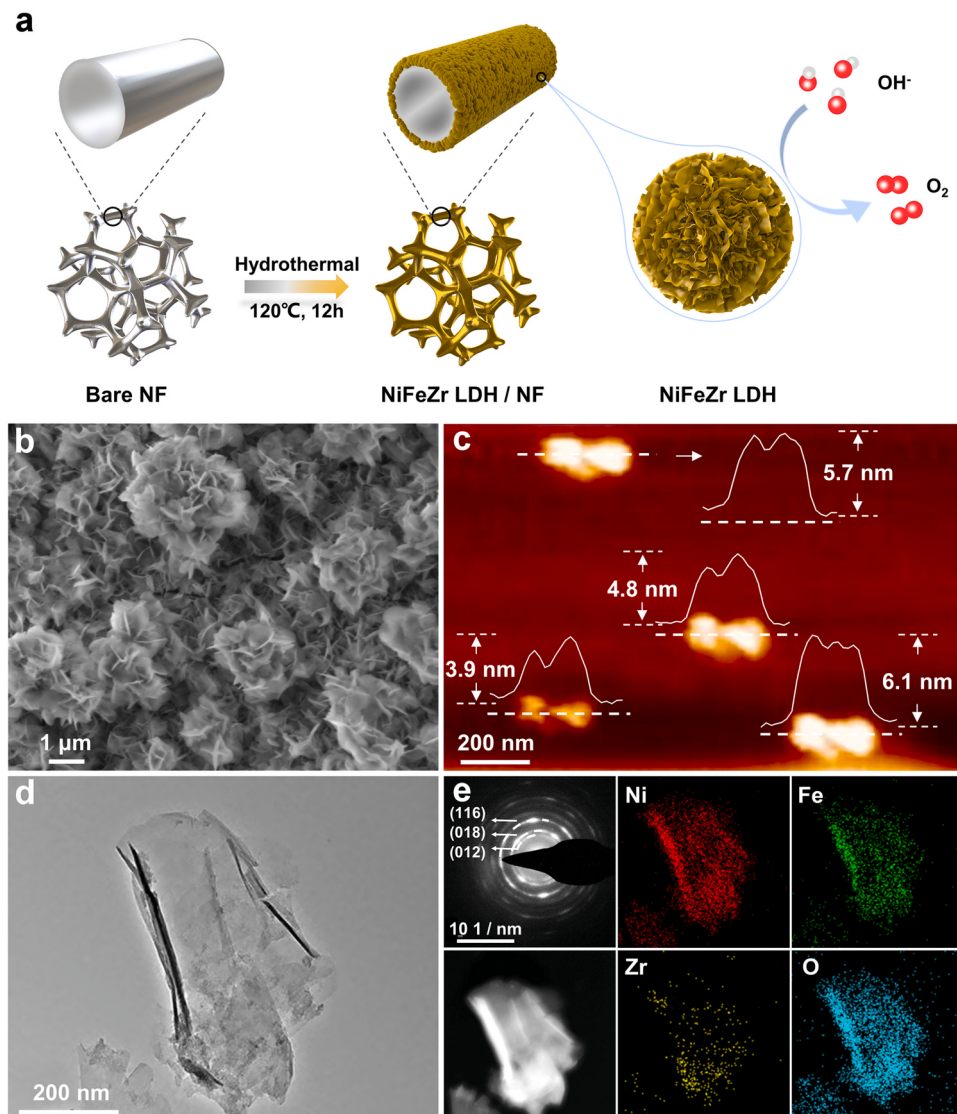


**Fig. 1.** (a) Schematic synthesis route for the NiFeZr LDH/NF electrode. (b) SEM image, (c) AFM image and the corresponding height curves, and (d) TEM image of NiFeZr LDH. (e) SADE pattern, HAADF-STEM image, and the corresponding EDX mapping of NiFeZr LDH.

the filled ( $t_{2g}$ )  $d$ -orbitals of  $\text{Ni}^{2+}$ , whereas the half occupied ( $t_{2g}$ )  $d$ -orbitals of  $\text{Fe}^{3+}$  interact with the bridging  $\text{O}^{2-}$  via a relatively weak  $\pi$ -donation after overlapping with the  $p$ -orbitals of  $\text{O}^{2-}$ , resulting in the partial electron transfer from  $\text{Ni}^{2+}$  to  $\text{Fe}^{3+}$  atoms [32]. Given the uniform distribution of elements, a Ni-O-Fe-O-Zr-O-Ni unit strongly interacts electronically among Ni, Fe, and Zr ions in NiFeZr LDH. Compared with  $\text{Ni}^{2+}$  and  $\text{Fe}^{3+}$ , the electron-unoccupied  $4d$ -orbitals of  $\text{Zr}^{4+}$  give rise to a relatively strong  $\pi$ -donation from the lone pair electrons of  $\text{O}^{2-}$  to  $\text{Zr}^{4+}$ , triggering efficient electron transfer. As a consequence, the  $\text{Zr}^{4+}$  dopant induces electron withdrawal from the parent Ni and Fe sites and modulates their electronic structure under strong electronic interaction [22]. In addition, the  $\text{Zr}^{4+}$  with unoccupied  $e_g$  orbitals can lead to too strong binding strength with absorbed oxygen species, whereas the  $\text{Fe}^{3+}$  and  $\text{Ni}^{2+}$  with half-occupied  $e_g$  orbitals tend to form relatively weak bonds with absorbed oxygen-containing intermediates on the surface [33,34]. According to the Sabatier principles, the moderate bonding strength between metal sites and adsorbed oxygen species is conducive to the release of reaction intermediates [35], which is responsible for the improved OER activity of the electrocatalyst.

### 3.3. Electrocatalytic OER performance

To evaluate the OER performance of LDH catalysts, electrochemical measurements were conducted in a three-electrode system in an oxygen-saturated electrolyte (1 M KOH) with a scan rate of  $5 \text{ mV s}^{-1}$  at room temperature. As shown in OER polarization curves (Fig. 3a), NiFeZr LDH exhibits a remarkable OER activity, delivering  $10 \text{ mA cm}^{-2}$  at the low overpotential ( $\eta$ ) of only 182 mV superior to those of NiFe LDH, NiZr LDH,  $\text{Ni}(\text{OH})_2$ , and commercial  $\text{RuO}_2$  (Table S2). To match the critical standard of industrial applications, the catalytic activity of NiFeZr LDH under large current densities were further evaluated. More encouragingly, it is unexpected that the electrode yields  $2000 \text{ mA cm}^{-2}$  under fairly low overpotentials of 314 mV (Fig. 3b). Evidently, in terms of whether low or high current densities, the OER performance of NiFeZr LDH is superior to the most recently reported state-of-the-art electrocatalysts (Fig. 3c-d and Tables S3-S4). The electrochemical surface area (ECSA) measurement was conducted to evaluate the exposed area of active sites (Figs. S6-S7 and Table S5). Similar to the trends of geometric area-normalized current density, NiFeZr LDH has the highest ECSA-normalized current density compared to other electrodes. In particular, NiFeZr LDH manifests a high current density of  $3.85 \text{ mA cm}^{-2}_{\text{ECSA}}$  at an overpotential of only 230 mV, indicating a much more favorable

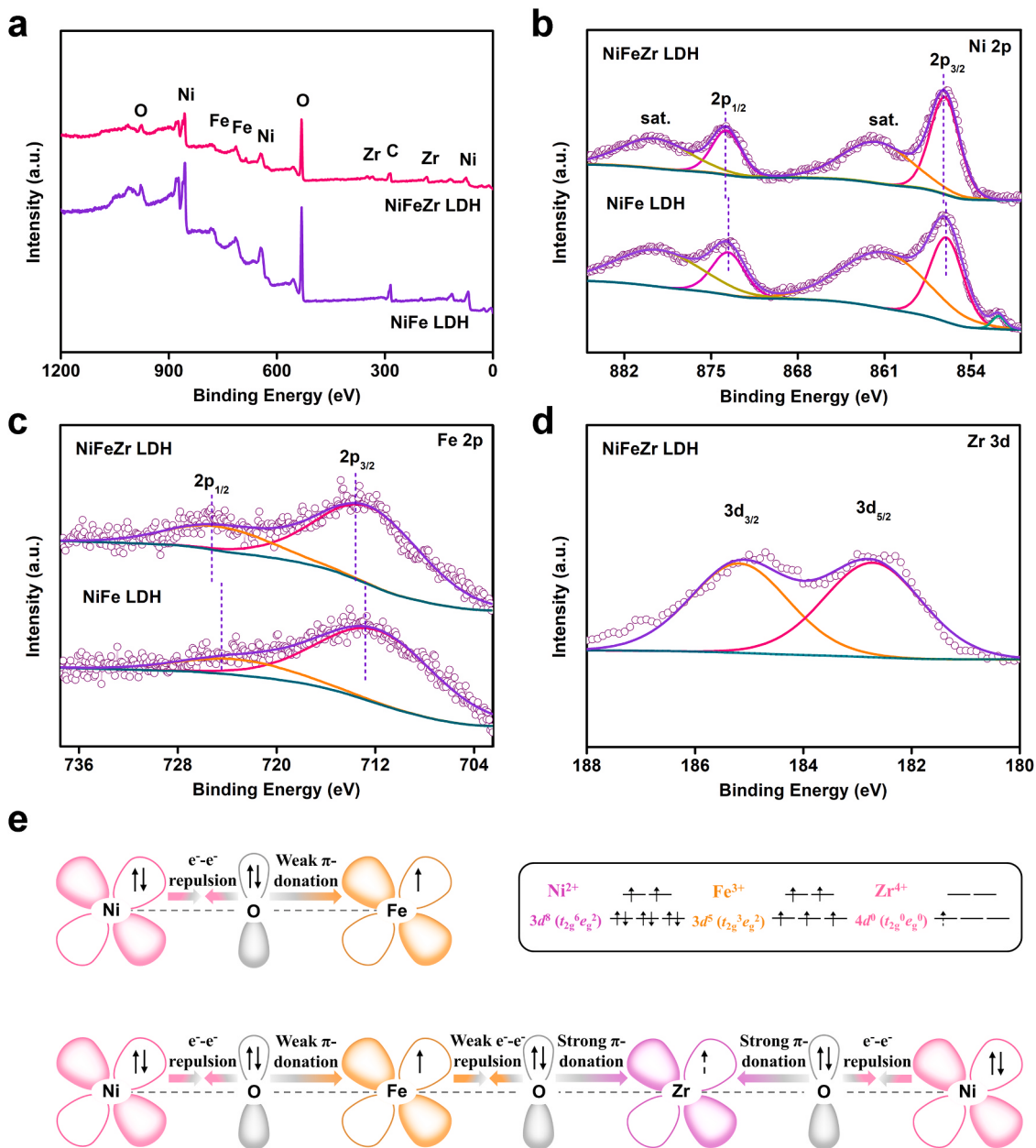


**Fig. 2.** Compositional characterization and interactions. (a) XPS spectral profiles for NiFeZr LDH and NiFe LDH, and the high-resolution XPS spectra of (b) Ni 2p, (c) Fe 2p, and (d) Zr 3d for NiFeZr LDH. (e) Schematic of the electronic interactions among Ni, Fe, Zr, and O in NiFe LDH and NiFeZr LDH.

intrinsic activity (Fig. 3e). To further distinguish the intrinsic activity of electrocatalysts, as shown in Fig. 3f, the turnover frequency (TOF) was examined according to ICP-MS data (Table S1). Noteworthy, NiFeZr LDH achieves an excellent TOF value of  $0.06\text{ s}^{-1}$  at only 216 mV, inherently surpassing those of NiFe LDH (298 mV), NiZr LDH (420 mV), and Ni(OH)<sub>2</sub> (467 mV), respectively. Consequently, it strongly implies the most intrinsically favored OER activity of NiFeZr LDH, which agrees with the ECSA-normalized current density analysis. Impressively, the NiFeZr LDH electrode exhibits robust stability over 750 h, even running for 550 h at large current densities of 500 and  $1000\text{ mA cm}^{-2}$  with negligible attenuation, further proving its superior industrial-grade OER performance (Fig. 3g).

#### 3.4. Electrochemical characterization

In addition to the intrinsic OER activity of active sites, the catalytic reaction kinetics and the exposure degree of active area are also key

factors to optimize OER performance. To probe the underlying kinetics mechanism, the Tafel slope and electrochemical impedance spectroscopy (EIS) of electrodes were investigated. As shown in Fig. 4a, the Tafel slope of NiFeZr LDH is only  $38.6\text{ mV dec}^{-1}$ , which is far lower than those of NiFe LDH, NiZr LDH, Ni(OH)<sub>2</sub>, and bare NF, indicating an inherently easier water oxidation reaction kinetics. In addition, the Nyquist plots based on EIS were performed to evaluate the charge-transfer resistance ( $R_{ct}$ ) at the electrode/electrolyte reaction interface. The  $R_{ct}$  value of NiFeZr LDH is about  $0.4\Omega$  versus  $2.0\Omega$  for NiFe LDH,  $13.4\Omega$  for NiZr LDH, and  $25.1\Omega$  for Ni(OH)<sub>2</sub>, revealing an extraordinary electric conductivity and more efficient charge transfer after doping Zr (Fig. 4b). Moreover, we investigated the carrier concentrations via Mott-Schottky curves (Fig. 4c) at open circuit voltage (OCP) and found that the NiFeZr LDH electrode also has the highest near-face carrier density of  $1.51 \times 10^{21}\text{ cm}^{-3}$  (Table S6), favorable to improve the OER kinetics. Due to the semiconductor properties of catalysts, the electrical conductivity is related to the bandgap [42]. The Zr dopant causes a much

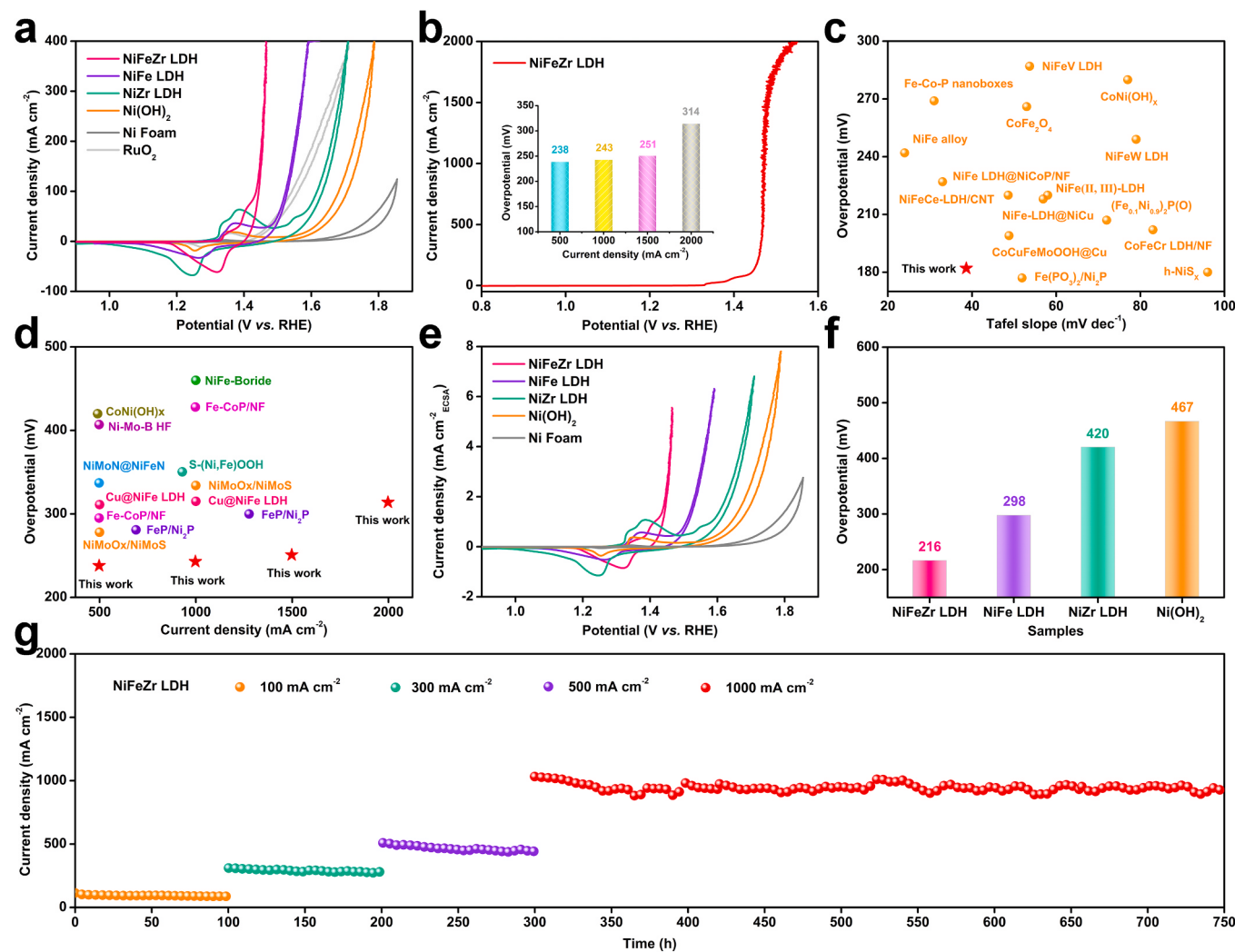


**Fig. 3.** Electrochemical measurements of NiFeZr LDH, NiFe LDH, NiZr LDH, and Ni(OH)<sub>2</sub>. (a), (b) OER polarization curves measured at a scan rate of 5 mV s<sup>-1</sup> in 1 M KOH electrolyte with 95% IR correction. Inset in (b) shows the overpotentials required at 500, 1000, 1500, and 2000 mA cm<sup>-2</sup> of NiFeZr LDH, respectively. (c), (d) Comparison of the overpotentials of NiFeZr LDH and other reported electrocatalysts at 10 mA cm<sup>-2</sup> condition [6,25,36–48] and large current densities [29,45, 49–55]. (e) The normalized current densities by ECSA. (f) The overpotentials required at TOF value of 0.06 s<sup>-1</sup>. (g) Long-term test under 100, 300, 500, and 1000 mA cm<sup>-2</sup> in 1 M KOH electrolyte.

narrower bandgap than the others, which also leads to an accelerated charge transfer process during OER (Figs. S8–S9).

To prove the relationships between the carrier concentration as well as the electrical conductivity and OER kinetics, the carrier concentrations and the bandgaps of NiFeZr LDH, NiFe LDH, NiZr LDH, and Ni(OH)<sub>2</sub> were described by the Tafel slope, respectively. As displayed in Fig. 4d, the carrier concentrations of electrocatalysts are negatively related to their Tafel slope, whereas the bandgap energies are opposite, confirming the enhanced water oxygen reaction kinetics of NiFeZr LDH. All these results illustrate that the introduction of Zr<sup>4+</sup> ions gives rise to much more favorable OER conditions while the electrochemical active areas of all catalysts when exposed to the solution are similar (Table S5). Therefore, the improved OER performance of NiFeZr LDH should be attributed to the admirable intrinsic electrocatalytic activity of each active site rather than the increased number of exposed active sites resulting from morphology optimization. In addition, the electronic structure of NiFe LDH and NiFeZr LDH after the durability test was investigated by XPS analysis (Figs. S10–S11). For NiFe LDH, the evident shift to the higher binding energy of Ni 2p and Fe 2p core level spectrum is observed, hinting that the surface Ni and Fe atoms are oxidized to higher valence states. As to NiFeZr LDH, the Ni 2p and Fe 2p binding energies are only slightly increased after the reaction, which indicates

that Zr plays a role in inhibiting the oxidation of surface Ni and Fe sites, contributing to the enhanced OER activity and robust stability.

### 3.5. Structural evolution mechanism identified by operando Raman

After the excellent OER activity and robust stability of NiFeZr LDH were demonstrated, a series of key questions regarding the catalytic mechanisms needed to be addressed. Therefore, the operando Raman spectroscopy was conducted to spectroscopically trace the structural evolution of NiFe LDH and NiFeZr LDH during the OER process to gain insight into the mechanisms taking place at the catalytic interfaces. As shown in Fig. 5a–b, under the open-circuit voltage (OCP), two representative peaks at around 457 and 527 cm<sup>-1</sup> are ascribed to E<sub>g</sub> bending and A<sub>1g</sub> stretching vibrations of Ni<sup>II</sup>-O, respectively [9]. The peaks that appear at 660–690 cm<sup>-1</sup> may be attributed to Fe<sup>III</sup>-O or Ni<sup>II</sup>-O-Fe<sup>III</sup> vibrations of NiFe LDH and NiFeZr LDH [56,57]. For NiFe LDH, with the applied potential increasing to 1.35 V, a pair of new Raman peaks appear at about 475 and 557 cm<sup>-1</sup>, which are attributed to Ni<sup>III</sup>-O vibration from the newly formed NiOOH phase (Fig. 5a) [20,58]. The evolution is verified by the first oxidation peak at about 1.33 V in the corresponding polarization curve (peak I, Fig. 5c). There may exist a mixture of  $\gamma$ -NiOOH and  $\beta$ -NiOOH phases due to the structural similarity

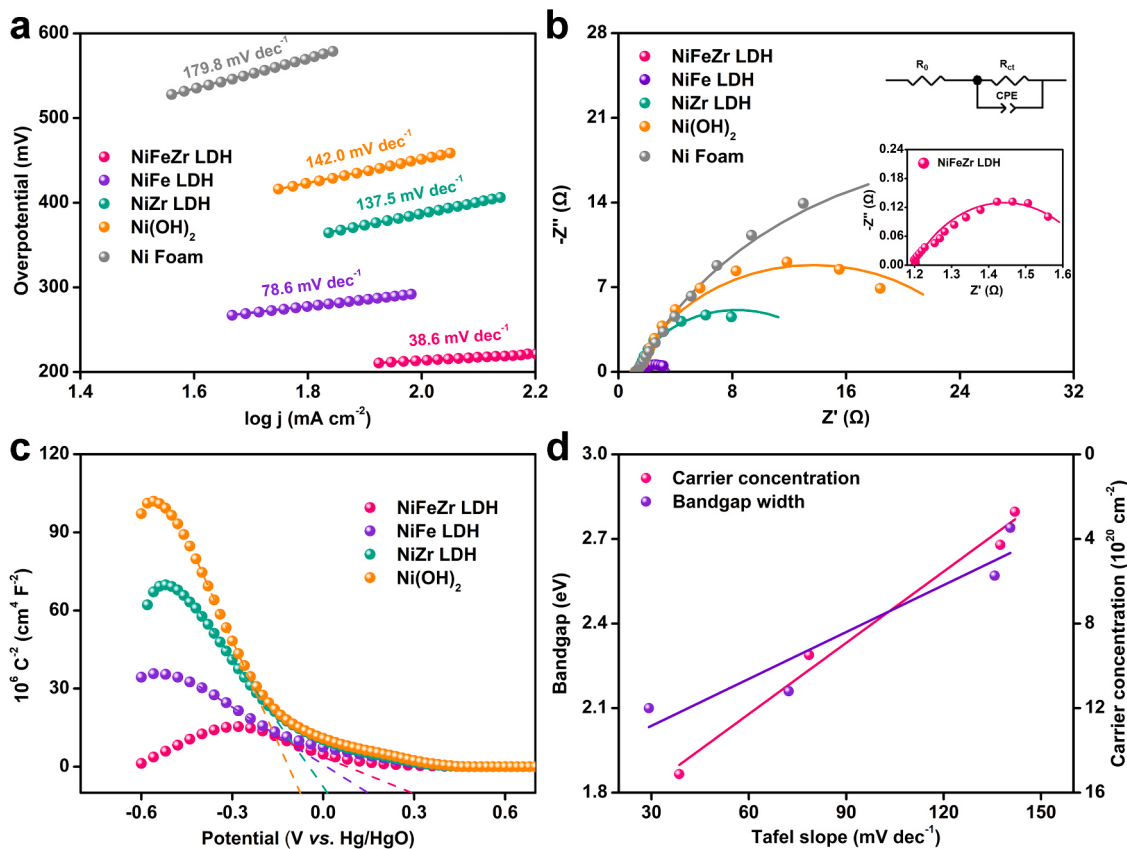


**Fig. 4.** Electrochemical properties of NiFeZr LDH, NiFe LDH, NiZr LDH, and Ni(OH)<sub>2</sub>. (a) Tafel plots. (b) Nyquist plots obtained at an applied potential of 1.5 V<sub>RHE</sub> without iR correction. Insets in (b) are the high-magnification plot of NiFeZr LDH and the equivalent circuit, respectively. (c) Mott-Schottky curves. (d) The relationship between Tafel slope and bandgap width as well as carrier concentration.

[22]. As to higher potentials ( $\geq 1.40$  V), the Ni<sup>III</sup>-O peaks gradually intensify, indicating the electrochemical oxidation transition from  $\beta$ -NiOOH to  $\gamma$ -NiOOH phase [59], as confirmed by the second oxidation peak at about 1.37 V in the curve (peak II, Fig. 5c). At 1.45 V, the intensity ratio of two Ni<sup>III</sup>-O peaks ( $I_{557}/I_{475}$ ) is about 0.73, which reveals the dominant  $\gamma$ -NiOOH phase at higher anodic potentials.

Fig. 5b shows that with the increased applied potential, NiFeZr LDH exhibits a consistent structural evolution with NiFe LDH. However, the new peaks assigned to Ni<sup>III</sup>-OOH appear until the applied potential increase to 1.38 V. Compared with NiFe LDH, the conversion of the Ni(OH)<sub>2</sub>/NiOOH redox pair in NiFeZr LDH is delayed, shifting to a higher potential about 1.34 V in the polarization curve (peak I, Fig. 5d). Under high anodic potentials ( $\geq 1.43$  V), the pair of Ni<sup>III</sup>-O peaks conducts oxidation evolution from  $\beta$ -NiOOH to  $\gamma$ -NiOOH phase, which corresponds to the second oxidation phenomenon at about 1.40 V in the polarization curve (peak II, Fig. 5d). At 1.48 V, the ratio of  $I_{557}/I_{475}$  reaches 0.93, indicating more  $\beta$ -NiOOH phase is generated in NiFeZr LDH compared to NiFe LDH. These results signify that Zr<sup>4+</sup> ions can inhibit the oxidation of Ni<sup>2+</sup> ions and restrain the phase transition from  $\beta$ -NiOOH to  $\gamma$ -NiOOH in the OER process. This difference in oxidation states of NiFe LDH and NiFeZr LDH matrix is consistent with the XPS analysis before and after the OER process (Figs. S10-S11). As revealed in Fig. 2e, the high-valence Zr<sup>4+</sup> with empty 4d-orbitals forms stronger covalent bonds with the bridge O atoms, leading to the electron withdrawal from parent Ni and Fe sites to the Zr<sup>4+</sup> dopants. Because Ni sites in NiFeZr LDH are electron deficient, more input energy would be needed to drive the oxidation reaction to generate NiOOH, which can cause the positive shift of anodic potential (peak I and peak II) and the suppressed oxidation of parent Ni and Fe atoms during OER [33]. The modulated electronic structure due to Zr<sup>4+</sup> dopant gives rise to the generation of more  $\beta$ -NiOOH phase, and it has been demonstrated that

$\beta$ -NiOOH active species with lower Ni oxidation states exhibit higher catalytic activity than the  $\gamma$ -NiOOH phase [60].

### 3.6. DFT calculations

While the electrochemical conversion pathway and active phase of NiFe LDH and NiFeZr LDH are elucidated by in-situ Raman spectroscopy, an atomic-level study is needed to address the active sites and the role of the Zr<sup>4+</sup> ions contributing to OER activity. First-principles DFT calculations were thus conducted to provide an insightful discussion. Herein, we selected (001) surface of NiFeZr LDH, NiFe LDH, and Ni(OH)<sub>2</sub> (Fig. S12), where the abundant unsaturated coordination metal ions at the edge can act as active sites (\*) [6,18]. Fig. 6a compares the cumulative Gibbs energy for OER involving intermediates (\*OH, \*O and \*OOH) on metal sites in the four-electron transfer process, deriving the theoretical overpotentials for NiFeZr LDH, NiFe LDH and Ni(OH)<sub>2</sub> catalysts (Table S7). The lowest theoretical overpotentials were found at Fe sites (\*Fe) in both NiFe LDH and NiFeZr LDH, rather than Ni sites (\*Ni) or Zr sites (\*Zr). The rate determining step (RDS) for OER at the Fe sites of both NiFe LDH and NiFeZr LDH is dehydrogenation of the surface hydroxyl (the second step, \*OH + OH<sup>-</sup>  $\rightarrow$  \*O + H<sub>2</sub>O + e<sup>-</sup>). The presence of Zr atoms offers the lowest overpotential of 0.47 V at the Fe active site of NiFeZr LDH, which is superior to those of NiFe LDH (0.59 V) or Ni(OH)<sub>2</sub> (0.85 V). NiFeZr LDH achieves an optimized reaction pathway, i.e., lowering the energy barrier for the conversion from OH\* to O\* at the Fe active sites during OER. The simulation provides a qualitative agreement with the experimental results shown in Fig. 3a.

The difference in Gibbs reaction energies of \*O and \*OH ( $\Delta G^*_{O-O}$ ) was adopted as a descriptor for the OER activity, which follows a volcano relation as shown in Fig. 6b. According to the linear restriction relationship shown in Fig. S13, the more  $\Delta G^*_{O-O}$ - $\Delta G^*_{OH}$  approaches to the

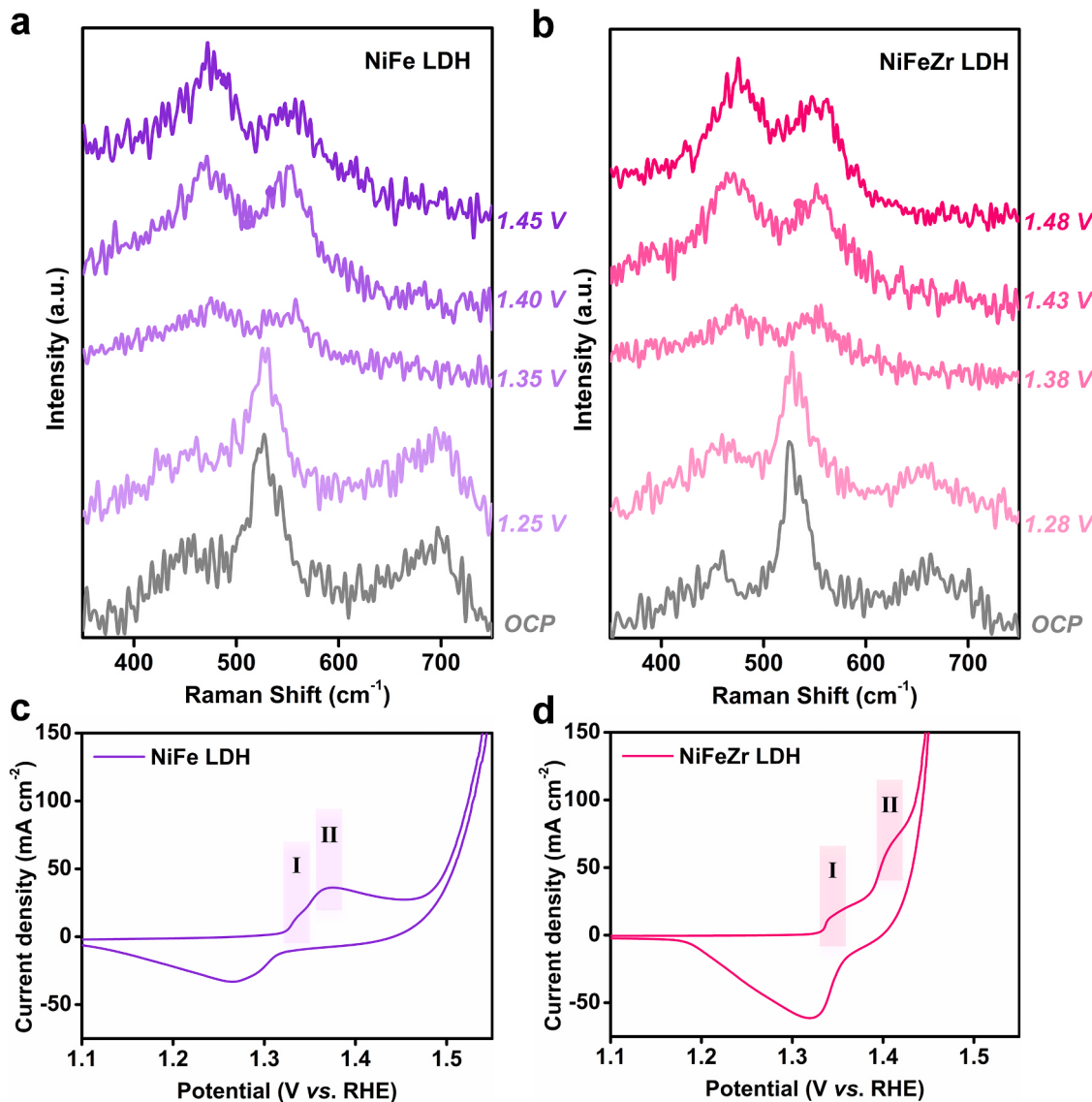


**Fig. 5.** Structural evolution of NiFe and NiFeZr catalysts during the electrocatalytic reaction. Raman spectra of (a) NiFe LDH and (b) NiFeZr LDH under applied potentials. The corresponding CV curves of (c) NiFe LDH and (d) NiFeZr LDH.

optimal value of 1.56 eV (the Gibbs reaction energy of the second and third steps, 3.13 eV divided by 2), the smaller the reaction overpotential is. The Fe sites provide optimal binding strength for the OER intermediates, yielding  $\Delta G_{\text{O}}^* - \Delta G_{\text{OH}}^*$  of 1.70 eV and 1.82 eV for NiFeZr LDH and NiFe LDH, respectively, with the overpotentials of 0.47 V and 0.59 V. Overall, the bonding strength of oxygen-containing species at the Fe sites follows the Sabatier principles [35]. However, the values of  $\Delta G_{\text{O}}^* - \Delta G_{\text{OH}}^*$  at the Ni sites are 2.08 eV and 2.27 eV for the two LDH catalysts, giving larger overpotentials of 0.85 V and 1.04 V for OER. Moreover, as shown in Fig. 6a, the RDS of OER at Zr sites of NiFeZr LDH lies in the third step ( $^*\text{O} + \text{OH}^- \rightarrow ^*\text{OOH} + \text{e}^-$ ), while the first two steps are energetically downhill and can occur spontaneously [20]. In comparison with the Ni and Fe sites, the Zr site is conducive to formation of the  $^*\text{O}$  species, resulting in a challenging energy barrier for formation of the  $^*\text{OOH}$  species and thus a limited reaction rate of OER [61]. Besides, as revealed by the density of states (DOS) in Fig. 6c, the Zr dopant contributes to a narrower bandgap due to additional spin-states generated below the conduction bands, which allow for improved electric conductivity and electron mobility as well as more favorable OER kinetics for NiFeZr LDH [42].

We calculated the Bader charges for the Fe active sites of NiFe LDH

and NiFeZr LDH to explore the underlying mechanism for the improved OER performance (Fig. 6d-e). In the beginning of the four-step oxidation cycle (defective surfaces in the left panels), the Fe sites of NiFe LDH and NiFeZr LDH show a reduced oxidation state with the Bader charge of 1.36e or 1.35e. As for the  $^*\text{OH}$ , a higher oxidation state is achieved for NiFe LDH with the Bader charge of 1.78e, whereas the lower oxidation state is maintained for NiFeZr LDH with that of 1.31e. The difference can be attributed to the electronic structure modulation of the  $\text{Zr}^{4+}$  dopant, which contributes more electrons into the matrix and prevents the oxidation of the Fe site. For the Fe sites in the  $^*\text{O}$  and  $^*\text{OOH}$  configurations, the higher oxidation state almost remains the same for NiFe LDH, but it increases first for NiFeZr LDH with the Bader charge of 1.61e and then decreases and recovers to 1.36e. For the RDS of OER on the two LDHs, the key lies in the  $^*\text{OH}$  species, where the higher oxidation state appears for the Fe site of NiFe LDH but a lower one for that of NiFeZr LDH. The difference in the Fe oxidation state leads a stronger binding interaction of the hydroxyl to the Fe site on NiFe LDH but a weaker binding interaction on NiFeZr LDH, and thus a larger and smaller Gibbs reaction energy for the RDSs on the two LDHs. As a consequence, the oxidation cycle at the Fe active sites is optimized after incorporating  $\text{Zr}^{4+}$  ions, thus enhancing the OER catalytic activity.

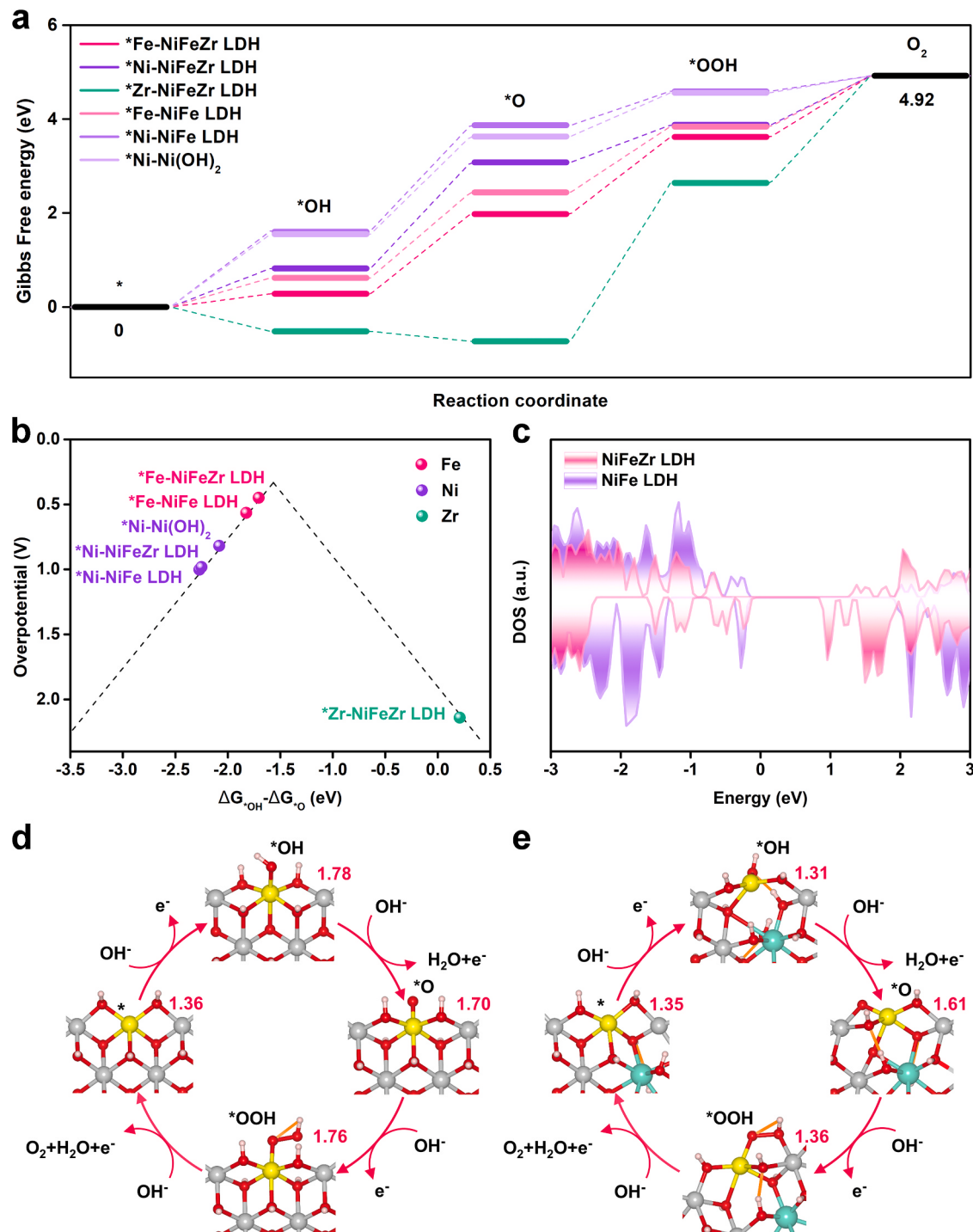


**Fig. 6.** DFT based first-principles calculations. (a) Gibbs energy profiles for OER at metal sites and (b) OER volcano relation based on calculated overpotentials for  $\text{Ni}(\text{OH})_2$ , NiFe LDH, and NiFeZr LDH at  $T = 298$  K. (c) Density of states (DOS) for NiFe LDH and NiFeZr LDH. OER cycle of (d) NiFe LDH and (e) NiFeZr LDH with marked Bader charge of Fe active site in yellow (Ni, gray; Zr, green; O, red; H, pink).

#### 4. Conclusions

To meet the industrial standard of high-current-density water electrolysis, we synthesized a novel NiFeZr LDH/NF electrode, which demonstrates an intrinsically exceptional OER performance by modulating the oxidation states of the NiFe LDH matrix via incorporating high-valence Zr dopant. NiFeZr LDH possesses an overpotential of 182 mV at the current density of  $10 \text{ mA cm}^{-2}$  and shows a Tafel slope of  $38.6 \text{ mV dec}^{-1}$ , which performs among the most superior NiFe-based electrocatalysts. It even achieves an industrial-grade current density of

$2000 \text{ mA cm}^{-2}$  at an extremely low overpotential of 314 mV and displays robust durability over 750 h of active water splitting. In the OER process, the NiOOH active phase was probed by tracking the structural evolution of the precatalyst with in-situ Raman spectroscopy. It was found that the  $\text{Zr}^{4+}$  ions retarded the electrochemical oxidation of  $\text{Ni}^{II}-\text{O}$  and induced more  $\beta$ -NiOOH phases with higher catalytic activity. DFT calculations reveal that Fe sites provide the most favorable reaction pathway and serve as active sites in NiFe LDH and NiFeZr LDH. The  $\text{Zr}^{4+}$  ions as electronic structure modulators optimize the binding strength of Fe active sites to OER intermediates and the oxidation cycle energy

during OER, significantly enhancing catalytic activity. The presented NiFeZr LDH electrocatalyst provides many advantages such as facile synthesis, low cost, high catalytic performance, and excellent durability. Our work may provide an avenue for designing more efficient LDH catalysts to bridge the gap between laboratory testing and industrial-grade requirements, especially for the economic production of hydrogen at high current densities on a large scale.

### CRediT authorship contribution statement

**Rui Zhao:** Investigation, Data curation, Formal analysis, Writing – original draft. **Shuai Xu and Dongyu Liu:** Formal analysis, Methodology, DFT calculation. **Liting Wei, Suyi Yang, and Xueli Yan:** Investigation, Resources, Data curation. **Yubin Chen, Zhaohui Zhou, and Clemens Burda:** Conceptualization, Project administration, Writing – review & editing. **Jinzhuan Su and Liejin Guo:** Writing – review & editing, Funding acquisition.

### Declaration of Competing Interest

The authors declare that they have no known competing financial interests or personal relationships that could have appeared to influence the work reported in this paper.

### Data availability

Data will be made available on request.

### Acknowledgements

The authors thank for the support from the National Natural Science Foundation of China (Nos. 51888103, 52076177), China National Key Research and Development Plan Project (No. 2021YFF0500503), Sichuan Science and Technology Program (No. 2021YFSY0047), and China Fundamental Research Funds for the Central Universities. C.B. acknowledges the College of Arts and Science of CWRU for supporting the Center for Chemical Dynamics and Nanomaterials Research.

### Appendix A. Supporting information

Supplementary data associated with this article can be found in the online version at [doi:10.1016/j.apcatb.2023.123027](https://doi.org/10.1016/j.apcatb.2023.123027).

### References

- [1] Z. Wang, J. Chen, E. Song, N. Wang, J. Dong, X. Zhang, P.M. Ajayan, W. Yao, C. Wang, J. Liu, J. Shen, M. Ye, Manipulation on active electronic states of metastable phase  $\beta$ -NiMoO<sub>4</sub> for large current density hydrogen evolution, *Nat. Commun.* 12 (2021) 5960.
- [2] C. Spöri, J.T.H. Kwan, A. Bonakdarpour, D.P. Wilkinson, P. Strasser, The stability challenges of oxygen evolving catalysts: Towards a common fundamental understanding and mitigation of catalyst degradation, *Angew. Chem. Int. Ed.* 56 (22) (2017) 5994–6021.
- [3] P.D. Luna, C. Hahn, D. Higgins, S.A. Jaffer, T.F. Jaramillo, E.H. Sargent, What would it take for renewable powered electrosynthesis to displace petrochemical processes? *Science* 364 (2019) 6438.
- [4] Q. Yu, Z. Zhang, S. Qiu, Y. Luo, Z. Liu, F. Yang, H. Liu, S. Ge, X. Zou, B. Ding, W. Ren, H.-M. Cheng, C. Sun, B. Liu, A Ta-Ta<sub>2</sub> monolayer catalyst with robust and metallic interface for superior hydrogen evolution, *Nat. Commun.* 12 (2021) 6051.
- [5] Y. Yao, S. Hu, W. Chen, Z.-Q. Huang, W. Wei, T. Yao, R. Liu, K. Zang, X. Wang, G. Wu, W. Yuan, T. Yuan, B. Zhu, W. Liu, Z. Li, D. He, Z. Xue, Y. Wang, X. Zheng, J. Dong, C.-R. Chang, Y. Chen, X. Hong, J. Luo, S. Wei, W.-X. Li, P. Strasser, Y. Wu, Y. Li, Engineering the electronic structure of single atom Ru sites via compressive strain boosts acidic water oxidation electrocatalysis, *Nat. Catal.* 2 (2019) 304–313.
- [6] L. Zhou, C. Zhang, Y. Zhang, Z. Li, M. Shao, Host modification of layered double hydroxide electrocatalyst to boost the thermodynamic and kinetic activity of oxygen evolution reaction, *Adv. Funct. Mater.* 31 (15) (2021) 2009743.
- [7] W.T. Hong, M. Risch, K.A. Stoerzinger, A. Grimaud, J. Suntivich, Y. Shao-Horn, Toward the rational design of non-precious transition metal oxides for oxygen electrocatalysis, *Energy Environ. Sci.* 8 (2015) 1404–1427.
- [8] D. Zhou, P. Li, X. Lin, A. McKinley, Y. Kuang, W. Liu, W.-F. Lin, X. Sun, X. Duan, Layered double hydroxide-based electrocatalysts for the oxygen evolution reaction: identification and tailoring of active sites, and superaerophobic nanoarray electrode assembly, *Chem. Soc. Rev.* 50 (2021) 8790–8817.
- [9] L. Peng, N. Yang, Y. Yang, Q. Wang, X. Xie, D. Sun-Waterhouse, L. Shang, T. Zhang, G.I.N. Waterhouse, Atomic cation-vacancy engineering of NiFe-layered double hydroxides for improved activity and stability towards the oxygen evolution reaction, *Angew. Chem. Int. Ed.* 60 (46) (2021) 24612–24619.
- [10] B. Zhang, L. Wang, Z. Cao, S.M. Kozlov, F.P.G. d Arquer, C.T. Dinh, J. Li, Z. Wang, X. Zheng, L. Zhang, Y. Wen, O. Voznyy, R. Comin, P.D. Luna, T. Regier, W. Bi, E. E. Alp, C.-W. Pao, L. Zheng, Y. Hu, Y. Ji, Y. Li, Y. Zhang, L. Cavallo, H. Peng, E. H. Sargent, High-valence metals improve oxygen evolution reaction performance by modulating 3d metal oxidation cycle energetics, *Nat. Catal.* 3 (2020) 985–992.
- [11] Z. Lu, H. Wang, D. Kong, K. Yan, P.-C. Hsu, G. Zheng, H. Yao, Z. Liang, X. Sun, Y. Cui, Electrochemical tuning of layered lithium transition metal oxides for improvement of oxygen evolution reaction, *Nat. Commun.* 5 (2014) 4345.
- [12] E. Fabbri, M. Nachtegaal, T. Binninger, X. Cheng, B.-J. Kim, J. Durst, F. Bozza, T. Graule, R. Schäublein, L. Wiles, M. Pertoso, N. Danilovic, K.E. Ayers, T. J. Schmidt, Dynamic surface self-reconstruction is the key of highly active perovskite nano-electrocatalysts for water splitting, *Nat. Mater.* 16 (2017) 925–931.
- [13] C. Li, X. Han, F. Cheng, Y. Hu, C. Chen, J. Chen, Phase and composition controllable synthesis of cobalt manganese spinel nanoparticles towards efficient oxygen electrocatalysis, *Nat. Commun.* 6 (2015) 7345.
- [14] R.P. Forslund, W.G. Hardin, X. Rong, A.M. Abakumov, D. Filimonov, C. T. Alexander, J.T. Mefford, H. Iyer, A.M. Kolpak, K.P. Johnston, K.J. Stevenson, Exceptional electrocatalytic oxygen evolution via tunable charge transfer interactions in  $\text{La}_{0.5}\text{Sr}_{1.5}\text{Ni}_{1-x}\text{Fe}_{x}\text{O}_{4\pm\delta}$  Ruddlesden-Popper oxides, *Nat. Commun.* 9 3150 (2018).
- [15] S. Klaus, M.W. Louie, L. Trotochaud, A.T. Bell, Effects of Fe electrolyte impurities on  $\text{Ni}(\text{OH})_2/\text{NiOOH}$  structure and oxygen evolution activity, *J. Phys. Chem. C.* 119 (13) (2015) 7243–7254.
- [16] D. Friebel, M.W. Louie, M. Bajdich, K.E. Sanwald, Y. Cai, A.M. Wise, M.-J. Cheng, D. Sokaras, T.-C. Weng, R. Alonso-Mori, R.C. Davis, J.R. Bargar, J.K. Norskov, A. Nilsson, A.T. Bell, Identification of highly active Fe sites in (Ni,Fe)OOH for electrocatalytic water splitting, *J. Am. Chem. Soc.* 137 3 (2015) 1305–1313.
- [17] H. Xiao, H. Shin, W.A. Goddard III, Synergy between Fe and Ni in the optimal performance of (Ni,Fe)OOH catalysts for the oxygen evolution reaction, *Proc. Natl. Acad. Sci. USA* 115 23 (2018) 5872–5877.
- [18] P. Li, X. Duan, Y. Kuang, Y. Li, G. Zhang, W. Liu, X. Sun, Tuning electronic structure of NiFe layered double hydroxides with vanadium doping toward high efficient electrocatalytic water oxidation, *Adv. Energy Mater.* 8 15 (2018) 1703341.
- [19] J. Lee, H. Jung, Y.S. Park, S. Woo, J. Yang, M.J. Jang, J. Jeong, N. Kwon, B. Lim, J. W. Han, S.M. Choi, High-efficiency anion-exchange membrane water electrolyzer enabled by ternary layered double hydroxide anode, *Small* 17 (28) (2021) 2100639.
- [20] X. Bo, R.K. Hocking, S. Zhou, Y. Li, X. Chen, J. Zhuang, Y. Du, C. Zhao, Capturing the active sites of multimetallic (oxy)hydroxides for the oxygen evolution reaction, *Energy Environ. Sci.* 13 (2020) 4225–4237.
- [21] J. Chen, H. Li, S. Chen, J. Fei, C. Liu, Z. Yu, K. Shin, Z. Liu, L. Song, G. Henkelman, L. Wei, Y. Chen, Co-Fe-Cr (oxy)hydroxides as efficient oxygen evolution reaction catalysts, *Adv. Energy Mater.* 11 11 (2021) 2003412.
- [22] M. Liu, K.-A. Min, B. Han, L.Y.S. Lee, Interfacing or doping? Role of Ce in highly promoted water oxidation of NiFe-layered double hydroxide, *Adv. Energy Mater.* 11 33 (2021) 2101281.
- [23] F. Qin, Z. Zhao, M.K. Alam, Y. Ni, F. Robles-Hernandez, L. Yu, S. Chen, Z. Ren, Z. Wang, J. Bao, Trimetallic NiFeMo for overall electrochemical water splitting with a low cell voltage, *ACS Energy Lett.* 3 (3) (2018) 546–554.
- [24] X. Wang, Y. Tuo, Y. Zhou, D. Wang, S. Wang, J. Zhang, Ta-doping triggered electronic structural engineering and strain effect in NiFe LDH for enhanced water oxidation, *Chem. Eng. J.* 403 (2021), 126297.
- [25] P.-F. Guo, Y. Yang, W.-J. Wang, B. Zhu, W.-T. Wang, Z.-Y. Wang, J.-L. Wang, K. Wang, Z.-H. He, Z.-T. Liu, Stable and active NiFeW layered double hydroxide for enhanced electrocatalytic oxygen evolution reaction, *Chem. Eng. J.* 426 (2021), 130768.
- [26] W. Liu, K. Jiang, Y. Hu, Q. Li, Y. Deng, J. Bao, Y. Lei, Zr-doped CoFe-layered double hydroxides for highly efficient seawater electrolysis, *J. Colloid Interface Sci.* 604 (2021) 767–775.
- [27] L. Huang, D. Chen, G. Luo, Y.-R. Lu, C. Chen, Y. Zou, C.-L. Dong, Y. Li, S. Wang, Zirconium-regulation-induced bifunctionality in 3D cobalt-iron oxide nanosheets for overall water splitting, *Adv. Mater.* 31 28 (2019) 1901439.
- [28] Y. Wang, W. Tang, X. Li, D. Wei, Improving the electrocatalytic activity of NiFe bimetal-organic framework toward oxygen evolution reaction by Zr doping, *Electrochim. Acta* 381 (2021), 138292.
- [29] H. Liu, X. Li, L. Chen, X. Zhu, P. Dong, M.O.L. Chee, M. Ye, Y. Guo, J. Shen, Monolithic Ni-Mo-B bifunctional electrode for large current water splitting, *Adv. Funct. Mater.* 32 4 (2021) 2107308.
- [30] L. Xu, S. Wu, X. He, H. Wang, D. Deng, J. Wu, H. Li, Interface engineering of anti-perovskite Ni<sub>3</sub>FeN/VN heterostructure for high-performance rechargeable zinc-air batteries, *Chem. Eng. J.* 437 (2022), 135291.
- [31] S. Wu, D. Deng, E. Zhang, H. Li, L. Xu, CoN nanoparticles anchored on ultra-thin N-doped graphene as the oxygen reduction electrocatalyst for highly stable zinc-air batteries, *Carbon* 196 (2022) 347–353.
- [32] J.Y.C. Chen, L. Dang, H. Liang, W. Bi, J.B. Gerken, S. Jin, E.E. Alp, S.S. Stahl, Operando analysis of NiFe and Fe oxyhydroxide electrocatalysts for water oxidation: Detection of Fe<sup>4+</sup> by Mössbauer spectroscopy, *J. Am. Chem. Soc.* 137 48 (2015) 15090–15093.

[33] D.A. Kuznetsov, B. Han, Y. Yu, R.R. Rao, J. Hwang, Y. Román-Leshkov, Y. Shao-Horn, Tuning redox transitions via inductive effect in metal oxides and complexes, and implications in oxygen electrocatalysis, Joule 2 (2) (2018) 225–244.

[34] C. Wei, Z. Feng, G.G. Scherer, J. Barber, Y. Shao-Horn, Z.J. Xu, Cations in octahedral sites: a descriptor for oxygen electrocatalysis on transition-metal spinels, *Adv. Mater.* 29 23 (2017) 1606800.

[35] J. Jiang, F. Sun, S. Zhou, W. Hu, H. Zhang, J. Dong, Z. Jiang, J. Zhao, J. Li, W. Yan, M. Wang, Atomic-level insight into super-efficient electrocatalytic oxygen evolution on iron and vanadium co-doped nickel (oxy)hydroxide, *Nat. Commun.* 9 (2018) 2885.

[36] W. Cai, R. Chen, H. Yang, H.B. Tao, H.-Y. Wang, J. Gao, W. Liu, S. Liu, S.-F. Hung, B. Liu, Amorphous versus crystalline in water oxidation catalysis: a case study of NiFe alloy, *Nano Lett.* 20 6 (2020) 4278–4285.

[37] Y. Zhou, Z. Wang, Z. Pan, L. Liu, J. Xi, X. Luo, Y. Shen, Exceptional performance of hierarchical Ni-Fe (hydr)oxide@NiCu electrocatalysts for water splitting, *Adv. Mater.* 31 8 (2019) 1806769.

[38] H. Zhang, X. Li, A. Hänel, V. Naumann, C. Lin, S. Azimi, S.L. Schweizer, A. W. Maijenburg, R.B. Wehrspohn, Bifunctional heterostructure assembly of NiFe LDH nanosheets on NiCoP nanowires for highly efficient and stable overall water splitting, *Adv. Funct. Mater.* 28 14 (2018) 1706847.

[39] Z. Wang, W. Liu, Y. Hu, M. Guan, L. Xu, H. Li, J. Bao, H. Li, Cr-doped CoFe layered double hydroxides: highly efficient and robust bifunctional electrocatalyst for the oxidation of water and urea, *Appl. Catal. B* 272 (2020), 118959.

[40] S. Lei, Q.-H. Li, Y. Kang, Z.-G. Gu, J. Zhang, Epitaxial growth of oriented prussian blue analogue derived well-aligned CoFe<sub>2</sub>O<sub>4</sub> thin film for efficient oxygen evolution reaction, *Appl. Catal. B* 245 (2019) 1–9.

[41] C. Lin, D. Wang, H. Jin, P. Wang, D. Chen, B. Liu, S. Mu, Construction of an iron and oxygen co-doped nickel phosphide based on MOF derivatives for highly efficient and long-enduring water splitting, *J. Mater. Chem. A* 8 (2020) 4570–4578.

[42] L. Zhang, W. Cai, N. Bao, Top-level design strategy to construct an advanced high-entropy Co-Cu-Fe-Mo (oxy)hydroxide electrocatalyst for the oxygen evolution reaction, *Adv. Mater.* 33 22 (2021) 2100745.

[43] H. Xu, B. Wang, C. Shan, P. Xi, W. Liu, Y. Tang, Ce-doped NiFe-layered double hydroxide ultrathin nanosheets/nanocarbon hierarchical nanocomposite as an efficient oxygen evolution catalyst, *ACS Appl. Mater. Interfaces* 10 7 (2018) 6336–6345.

[44] X. Li, B. Yang, Y. Wu, S. Lin, L. Zhang, Homogeneous Co<sub>3</sub>O<sub>4</sub> film electrode with enhanced oxygen evolution electrocatalysis via surface reduction, *Chin. J. Chem. Eng.* 29 (2021) 221–227.

[45] S. Li, Y. Wang, S. Peng, L. Zhang, A.M. Al-Enizi, H. Zhang, X. Sun, G. Zheng, Co-Ni-based nanotubes/nanosheets as efficient water splitting electrocatalysts, *Adv. Energy Mater.* 6 (2016) 1501661.

[46] B. You, Y. Sun, Hierarchically porous nickel sulfide multifunctional superstructures, *Adv. Energy Mater.* 6 7 (2016) 1502333.

[47] H. Zhou, F. Yu, J. Sun, R. He, S. Chen, C.-W. Chu, Z. Ren, Highly active catalyst derived from a 3D foam of Fe(PO<sub>3</sub>)<sub>2</sub>/Ni<sub>3</sub>P for extremely efficient water oxidation, *Proc. Natl. Acad. Sci. USA* 114 22 (2017) 5607–5611.

[48] H. Zhang, W. Zhou, J. Dong, X.F. Lu, X.W. (David), Lou, Intramolecular electronic coupling in porous iron cobalt (oxy)phosphide nanoboxes enhances the electrocatalytic activity for oxygen evolution, *Energy Environ. Sci.* 12 (2019) 3348–3355.

[49] L. Yu, L. Wu, B. McElhenney, S. Song, D. Luo, F. Zhang, Y. Yu, S. Chen, Z. Ren, Ultrafast room-temperature synthesis of porous S-doped Ni/Fe (oxy)hydroxide electrodes for oxygen evolution catalysis in seawater splitting, *Energy Environ. Sci.* 13 (2020) 3439–3446.

[50] P. Zhai, Y. Zhang, Y. Wu, J. Gao, B. Zhang, S. Cao, Y. Zhang, Z. Li, L. Sun, J. Hou, Engineering active sites on hierarchical transition bimetal oxides/sulfides heterostructure array enabling robust overall water splitting, *Nat. Commun.* 11 (2020) 5462.

[51] L. Yu, Q. Zhu, S. Song, B. McElhenney, D. Wang, C. Wu, Z. Qin, J. Bao, Y. Yu, S. Chen, Z. Ren, Non-noble metal-nitride based electrocatalysts for high-performance alkaline seawater electrolysis, *Nat. Commun.* 10 (2019) 5106.

[52] L.-M. Cao, Y.-W. Hu, S.-F. Tang, A. Iljin, J.-W. Wang, Z.-M. Zhang, T.-B. Lu, Fe-CoP electrocatalyst derived from a bimetallic prussian blue analogue for large-current-density oxygen evolution and overall water splitting, *Adv. Sci. S* 5 10 (2018) 1800949.

[53] F. Yu, H. Zhou, Y. Huang, J. Sun, F. Qin, J. Bao, W.A. Goddard III, S. Chen, Z. Ren, High-performance bifunctional porous non-noble metal phosphide catalyst for overall water splitting, *Nat. Commun.* 9 (2018) 2551.

[54] N. Wang, A. Xu, P. Ou, S.-F. Hung, A. Ozden, Y.-R. Lu, J. Abed, Z. Wang, Y. Yan, M.-J. Sun, Y. Xia, M. Han, J. Han, K. Yao, F.-Y. Wu, P.-H. Chen, A. Vomiero, A. Seifitokaldani, X. Sun, D. Sinton, Y. Liu, E.H. Sargent, H. Liang, Boride-derived oxygen-evolution catalysts, *Nat. Commun.* 12 (2021) 6089.

[55] L. Yu, H. Zhou, J. Sun, F. Qin, F. Yu, J. Bao, Y. Yu, S. Chen, Z. Ren, Cu nanowires shelled with NiFe layered double hydroxide nanosheets as bifunctional electrocatalysts for overall water splitting, *Energy Environ. Sci.* 10 (2017) 1820–1827.

[56] K. Dastafkan, S. Wang, C. Rong, Q. Meyer, Y. Li, Q. Zhang, C. Zhao, Cosynergistic molybdate oxo-anionic modification of FeNi-based electrocatalysts for efficient oxygen evolution reaction, *Adv. Funct. Mater.* 32 5 (2022) 2107342.

[57] C. Liang, P. Zou, A. Nairan, Y. Zhang, J. Liu, K. Liu, S. Hu, F. Kang, H.J. Fan, C. Yang, Exceptional performance of hierarchical Ni-Fe oxyhydroxide@NiFe alloy nanowire array electrocatalysts for large current density water splitting, *Energy Environ. Sci.* 13 (2020) 86–95.

[58] Y.-j. Wu, J. Yang, T.-x. Tu, W.-q. Li, P.-f. Zhang, Y. Zhou, J.-f. Li, J.-t. Li, S.-G. Sun, Evolution of cationic vacancy defects: A motif for surface restructuration of OER precatalyst, *Angew. Chem. Int. Ed.* 60 (51) (2021) 26829–26836.

[59] B.S. Yeo, A.T. Bell, In situ Raman study of nickel oxide and gold-supported nickel oxide catalysts for the electrochemical evolution of oxygen, *J. Phys. Chem. C* 116 15 (2012) 8394–8400.

[60] M.W. Louie, A.T. Bell, An investigation of thin-film Ni-Fe oxide catalysts for the electrochemical evolution of oxygen, *J. Am. Chem. Soc.* 135 33 (2013) 12329–12337.

[61] P. Liao, J.A. Keith, E.A. Carter, Water oxidation on pure and doped hematite (0001) surfaces: prediction of Co and Ni as effective dopants for electrocatalysis, *J. Am. Chem. Soc.* 134 32 (2012) 13296–13309.